

Effects of particle collisions on motions of mixed-size particles and bed structures

T. Fukuda & S. Fukuoka

Research and Development Initiative, Chuo University, Bunkyo-ku, Tokyo, Japan

ABSTRACT: Gravel-bed rivers display a large variety of particle sizes and shapes. However, effects of collisions among particles in different sizes on particle motions and bed structures are hardly clarified. This paper presents results of a numerical simulation with a numerical movable-bed channel capable of simulating three-dimensional motions of flows and particles in different sizes and shapes. The numerical simulation revealed differences in action directions of contact forces of particles in different sizes and effects of particle-volume concentrations on particle collisions. The simulation also demonstrated that collisions among particles in different sizes strongly affected particle motions and vertical structures of the movable bed.

1 INTRODUCTION

Sediment transports in gravel-bed rivers depend on particle characteristics such as sizes, shapes and bed structures. Large gravel particles exposed on bed surfaces were considered to resist mainly against hydrodynamic forces during floods and reduce entrainment of small particles from the river bed (Osada & Fukuoka 2010, Fukuoka & Abe 2007). Large-particle clusters were found to increase river-bed stabilities by observations in gravel-bed rivers (Hendrick et al. 2010). Many researchers have investigated sediment-transport mechanism in gravel-bed rivers. However, their mechanisms have not been clarified sufficiently because motions of particles could be hardly measured in flood flows.

The progress in computer processors made possible to investigate to sediment-transport mechanism by numerical approaches in which particle motions were simulated by a Lagrangian method (Truong et al. 2007, Harada et al. 2013). Fluid motions were simulated by the governing equations of one-fluid model for solid-liquid multiphase flows in an Eulerian method and particle motions were simulated by the Distinct Element Method. This numerical method can predict fluid forces acting on particles directly by simulating fluid motions around particles in detail using smaller computational cells than particle sizes. Most studies in the Lagrangian method have modeled particles as a single sphere. Therefore, it was unable to discuss important effects of sizes and shapes of particles on vertical structures of movable beds such as sorting and imbrications seen commonly in gravel-bed rivers (Millane et al. 2006).

We developed a numerical model (numerical movable-bed channel) capable of simulating motions of flows and particles in different sizes and shapes which were made by the superposition of several small spheres, as shown in Figure 1 (Fukuda et al. 2012, Fukuda et al. 2013). Sediment-transport equations are generally derived by using hydrodynamic forces. However, the numerical movable-bed experiment revealed that particles frequently started to shift by collisions with particles moving down from upstream. These facts told us that appropriate considerations of particle collisions as well as hydrodynamic forces were essential for prediction methods of sediment transports in gravel-bed rivers.

The present paper first explains a development process of bed topographies of antidunes caused by sorting of particles and forming large-particle clusters in the numerical channel, and then demonstrates dynamic features of collisions of large particles and small particles and effects of collisions on particle motions and bed structures.

Eulerian equations of particle motions are practical for simulating sediment transports over a



Figure 1. Shapes of model particles and real gravel particles.

large area. However, the Eulerian approach seems to be difficult to incorporate properly dynamics of particle collisions at present. Thus, establishing Eulerian equations of particle motions based on results of Lagrangian particle motions in the numerical movable-bed channel is required for predictions of bed variations in gravel-bed rivers. Stresses of particle collisions must be estimated for this purpose. Time and space averaging of particle collisions and averaging collision forces acting on a unit area are necessary for estimation of stresses of particle collisions. However, studies estimating stresses of particle collisions based on simulated Lagrangian particle motions showed to be small variations of particle motions in space and time (Harada et al. 2013). It was caused by numerical computations of small simulation regions for large computational load.

The present numerical channel was long (15 m) to discuss relationships among particle motions, particle collisions, and bed structures under a condition where particle sorting and bed waves were formed. Estimating stresses of particle collisions is difficult under these nonuniform conditions. Therefore, we focus on not stresses of particle collisions but forces acting on each particle directly and investigate contact forces on particles in different sizes. Then, relationships among particle collisions, Lagrangian particle motions and bed structures are discussed in the numerical movable-bed channel.

2 NUMERICAL METHOD

2.1 Governing equations of fluid motions

In the simulation of fluid motions, liquid and solid were simulated as an incompressible multiphase flow where regions of gravel particles were considered as fluids having densities different from water (Ushijima et al. 2008). Smagorinsky model was used as the subgrid turbulence model:

$$\frac{\partial u_i}{\partial x_i} = 0 \quad (1)$$

$$\frac{\partial u_i}{\partial t} + u_j \frac{\partial u_i}{\partial x_j} = g_i - \frac{1}{\rho} \frac{\partial P}{\partial x_i} + \frac{\partial}{\partial x_j} \left\{ 2(\nu + \nu_t) S_{ij} \right\} \quad (2)$$

$$\nu_t = (C_s \Delta)^2 \sqrt{2S_{ij}S_{ij}} \quad (3)$$

where u_i : i -th component of averaged velocity of a fluid computational cell including gravel particles, ρ : density, P : sum of pressure and isotropic component of SGS stresses, g : gravitational acceleration, S_{ij} : strain rate tensors, ν : kinematic viscosity, ν_t : SGS turbulent viscosity, C_s : Smagorinsky constant,

and Δ : computational cell size. Physical property ϕ (density ρ , dynamic viscosity μ) and averaged velocity u_i were computed as volume-averaged values and mass-averaged values, respectively.

Water surfaces were simulated by computing advection of water volume fractions in fluid computational cells with the Donor Cell Method.

2.2 Model particles with different sizes and shapes

Particles of various sizes and shapes were made by the superposition of several small spheres (Matsushima et al. 2009) to detect contact and collision points between particles, as seen in Figure 1. It was difficult to compute geometrical shapes of lapped part of spheres, therefore, computations of rigid body properties such as mass, gravity centers, and tensor of momentum inertia become important. We computed rigid body properties of particles by using sufficiently small cells and integrating numerically volumes and points of cells included in individual particles. Rigid body properties of particles do not change in motion, therefore, they were computed only once at the beginning of the simulation for every particles.

2.3 Governing equations of particle motions in flows

Particle motions were simulated by the momentum equations and the angular momentum equations of rigid bodies:

$$M\ddot{\mathbf{r}}_g = M\mathbf{g} + \mathbf{F}_f + \mathbf{F}_c \quad (4)$$

$$\dot{\boldsymbol{\omega}}_r = \mathbf{I}_r^{-1} \left\{ \mathbf{R}^{-1} (\mathbf{N}_f + \mathbf{N}_c) - \boldsymbol{\omega}_r \times \mathbf{I}_r \boldsymbol{\omega}_r \right\} \quad (5)$$

where bold face letters indicate vector, tensor, and matrix, M : mass of particle, \mathbf{r}_g : position of center of gravity, \mathbf{F} : force acting on a particle surface, \mathbf{N} : torque acting on particles, $\boldsymbol{\omega}$: angular velocity, \mathbf{R} : transformation matrix (from the local coordinates system to the global coordinates system), and \mathbf{I} : tensor of momentum inertia. Suffixes f and c are fluid force and contact force, respectively, and suffix r is components in local coordinates systems of each particle. In solving angular momentum equations, next time step angular velocities in local coordinates system $\boldsymbol{\omega}_r$ were first solved with eq. (5). Then, angular velocities in global coordinates system $\boldsymbol{\omega}$ were computed with transformation matrices \mathbf{R} . Next time step transformation matrices \mathbf{R} were set in consideration of rotations in time step Δt with the angular velocities $\boldsymbol{\omega}$. Next time step small sphere positions were set with next time step transformation matrices \mathbf{R} and small sphere positions in local coordinates system. In these coordinates transformation between global

coordinates system and local coordinates system, quaternions were used instead of transformation matrix \mathbf{R} (Ushijima et al. 2008).

2.4 Fluid force

Fluid forces acting on a particle are estimated with integrating forces acting on a particle region in the multiphase flow (Ushijima et al. 2008):

$$F_{f,i} = \int_{\Omega_s} \left\{ -\frac{\partial P}{\partial x_i} + \rho \frac{\partial}{\partial x_j} \{ 2(\nu + \nu_t) S_{ij} \} \right\} d\Omega \quad (6)$$

$$N_{f,i} = \int_{\Omega_s} \varepsilon_{ijk} r_{f,j} \left\{ -\frac{\partial P}{\partial x_k} + \rho \frac{\partial}{\partial x_l} \{ 2(\nu + \nu_t) S_{kl} \} \right\} d\Omega \quad (7)$$

where $F_{f,i}$: i -th component of fluid force, $N_{f,i}$: i -th component of torque caused by fluid force, $r_{f,i}$: position vector from a center of gravity of a particle to a fluid computational cel, Ω_s : region occupied by a particle, and ε_{ijk} : Levi-Civita symbol.

2.5 Contact forces

Contact forces acting among particles are computed by contact detections of each small sphere composing a particle. Contact forces and torques act on centers of gravity of particles. They are computed by the summation of computed contact forces concerning each small sphere:

$$\mathbf{F}_c = \sum_n \mathbf{F}_{cp,n}, \quad \mathbf{N}_c = \sum_n \mathbf{r}_{cp,n} \times \mathbf{F}_{cp,n} \quad (8)$$

where, \mathbf{F}_c and \mathbf{N}_c are contact force and torque acting on center of gravity of a particle, respectively. $\mathbf{F}_{cp,n}$ is contact force acting on each small sphere, and $\mathbf{r}_{cp,n}$ is position vector from particle's center of gravity to a contact point. Contact forces among particles were simulated by the Distinct Elements Method (Cundall & Strack 1979). Spring constants k and coefficients of dashpots c were computed by equations (9)–(11) (Tsuji et al. 1992):

$$k_n = \left\{ \frac{4}{9} \left(\frac{r_1 r_2}{r_1 + r_2} \right) \left(\frac{E}{1 - pos^2} \right)^2 e_n \right\}^{\frac{1}{3}} \quad (9)$$

$$s_0 = \frac{k_s}{k_n} = \frac{1}{2(1 + pos)} \quad (10)$$

$$c_n = 2h \sqrt{\frac{m_1 m_2}{m_1 + m_2}} k_n, \quad c_s = c_n \sqrt{s_0} \quad (11)$$

where e : spring force, E : Elastic modulus, pos : Poisson's ratio, h : dashpot coefficient, r_1 and r_2 : radii of two contacting spheres, m_1 and m_2 : mass of contacting spheres, and suffixes n and s : components of directions from center of a sphere to the contact point and orthogonal two directions on the tangential plane, respectively.

3 NUMERICAL MOVABLE-BED EXPERIMENT

The numerical movable-bed channel and the definition of coordinates system used in the analysis are shown in Figure 2. The numerical channel was 15 m long, 1 m wide with a bed slope of 1:20 and large enough to transport gravel particles, sufficiently long for sand waves to form, and accommodated to computation load. Five different sizes

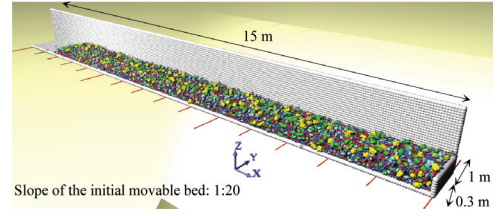


Figure 2. Numerical movable-bed channel and definition of coordinates system.

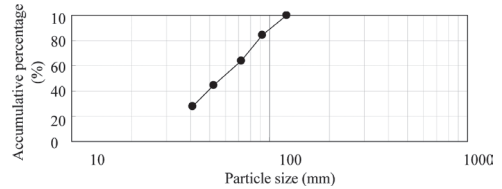


Figure 3. Particle size distribution.

Table 1. Parameters used in the simulation.

$\Delta x, \Delta y, \Delta z$: Fluid-computational cell size	0.01	m
Δt : Time step for fluid simulation	1.0×10^{-4}	s
$\Delta t'$: Time step for particle simulation	1.0×10^{-6}	s
ρ_w : Density of water	1,000	kg/m ³
ρ_p : Density of particles	2,650	kg/m ³
μ_w : Viscosity coefficient of water	8.9×10^{-4}	Pa · s
μ_p : Viscosity coefficient of particles	8.9×10^{-4}	Pa · s
C_s : Smagorinsky constant	0.173	
E : Elastic modulus	5.0×10^{10}	Pa
pos : Poisson's ratio	0.33	
h : Dashpot coefficient	0.11	

of particles (40 mm, 50 mm, 70 mm, 90 mm, and 120 mm) with four different shapes of gravel particles as shown in Figure 1 were made by varying sizes of small spheres and by superimposing them properly. Diameters of different shape particles were estimated as diameters of spheres with the same volume. In this paper we defined particles more than 90 mm as larger particles and less than 70 mm as smaller particles. The particle size distribution of the numerical channel bed was given by that as shown in Figure 3. Then the channel was made by dropping a set of particles with the size distribution randomly and repeatedly. A discharge of 0.5 m³/s was supplied at the upstream end of the channel and zero-pressure was given at the downstream end. The numerical movable-bed experiment was lasted for 400 s. It took about 3 months by the computation using shared memory systems (64 core: Intel Xeon E7-8837 (2.67 GHz) 8 core × 8). The parameters used in the simulation are shown in Table 1.

4 RESULTS OF NUMERICAL MOVABLE-BED EXPERIMENTS

4.1 Variations of sediment-transport rates and hydrodynamic forces with development of antidune

Temporal variations in longitudinal profiles of laterally averaged-bed levels and water-surface levels are shown in Figure 4. The values were averaged for two seconds because flow fields frequently changed in a second due to turbulence. The flow was supercritical and water surface profiles varied in the same phase as bed waves. Temporal variations of the bed surface are shown in Figure 5. Beds at the beginning of the numerical experiment were plane and changed into antidunes after $t = 300$ s. Antidunes moved upstream between $t = 300$ s and 400 s. Variations in hydraulic conditions every 100 seconds are shown in Table 2. The table shows values of maximum, minimum, and cross-sectional average in terms of depth, velocity, and Froude number measured from $x = 6$ m to $x = 15$ m. Differences between the maximum and minimum values of depths,

velocities, and Froude numbers became greater with the elapsed time.

Sediment-transport rates of particles in different sizes and in total measured at the downstream end of the channel are shown in Figure 6. The figure shows that the total sediment-transport rate decreased with time. Sediment-transport rates of larger particles were more than twice as large as that of smaller particles before the development of antidunes, however, they became almost the same after the development of antidunes ($t = 300$ s). Depositions of sediment on upstream slopes of antidunes (in $t = 300$ s – 400 s at $x = 3$ m, 6 m, and 13.5 m, as shown in Fig. 4) decreased sediment-transport rates, and scourings at downstream slopes of antidunes (in $t = 300$ s – 400 s at $x = 4.5$ m, 9 m, and 12 m) increased them. Sediment depositions and scourings did not necessarily occur at the same time. Therefore, sediment-transport rates greatly varied with time after development of antidunes.

Hydrodynamic forces acting on the bed were computed to investigate effects of antidunes on the motions of flows and particles. Figure 7 shows distributions of hydrodynamic forces acting on movable-bed in a unit area at $t = 100$ s and 400 s. These values were evaluated by converting hydrodynamic forces to shear stresses $\tau_{f,zx}$. The converted forces $\tau_{f,zx}$ were calculated by eq. (12). The region of integrations is from the channel bottom to the top of moving particles in the 0.01 m × 0.01 m area on the x - y plane.

$$\tau_{f,zx} = \frac{\iiint \alpha \left\{ -\frac{\partial P}{\partial x_1} + \rho \frac{\partial}{\partial x_j} \left\{ 2(\nu + \nu_i) S_{1j} \right\} \right\} dx dy dz}{\iint dx dy} \quad (12)$$

where α is a volume fraction of particles in a fluid computational cell.

Figure 7 shows that large hydrodynamic forces acted sparsely on large particles exposed on the bed surface at $t = 100$ s before the development of antidunes. On the other hand, large hydrodynamic forces after the development of antidunes ($t = 400$ s)

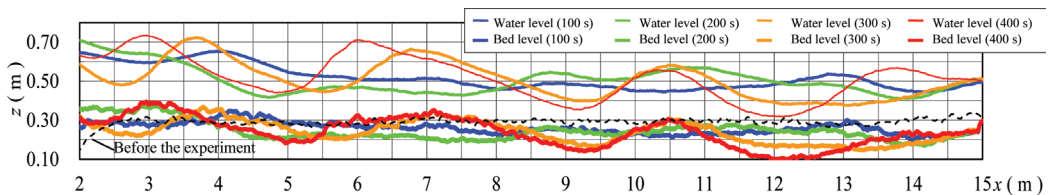


Figure 4. Longitudinal profiles of laterally averaged water-surface levels and bed levels.

were seen on the bed of $x = 3-4$ m, $x = 7-8$ m, and $x = 11-12$ m. They were concentrated on antidunes. The mean velocities in the channel center averaged in $t = 390$ s \sim $t = 400$ s are shown in Figure 8. Large hydrodynamic forces concentrated on downstream slopes of antidunes where flows near the bed were accelerated as shown in Figures 7 and 8. We averaged hydrodynamic forces acting on particles in a unit area over $x = 6$ m to $x = 15$ m. A temporal variation of averaged hydrodynamic forces on particles in a unit area is shown in Figure 9. Hydrodynamic forces acting on the bed after development of antidunes (after $t = 300$ s) were larger than those of the initial stage. The comparison between sediment-transport rates (Fig. 6) and hydrodynamic forces (Fig. 9) shows that sediment-transport rates in the final stage were smaller than those of the initial stage while hydrodynamic forces in the final stage were greater. This demonstrates that the sediment-transport rate was controlled by not only hydrodynamic forces acting on bed surfaces but also

bed structures. A temporal variation of particle size distributions on the bed surface is shown in Figure 10. When hydrodynamic forces were a minimum at $t = 200$ s (Fig. 9), the particle size distribution on the bed surface was a little smaller than that of the initial but almost the same. When antidunes developed ($t = 400$ s), the rate of large particles on the bed surface were not necessarily great. Thus, the reason why hydrodynamic forces increased at $t = 400$ s was not due to increasing the percentage of large particles on the bed surface. It was because antidune formation increased the resistance of the bed and decreased sediment-transport rates.

4.2 Vertical structures of antidune beds

A distribution of particle-volume concentrations in the center of the channel in $t = 400$ s is shown in Figure 11. Particle-volume concentrations were computed by counting the number of small cells (0.005^3 m³) occupied by particles in a region (0.4 m square and 0.01 m height) as illustrated in Figure 12 and dividing the number by the total number of cells in the region. We set a region with the height of 0.01 m to evaluate detailed distributions changing greatly in the vertical direction. The figure indicates particle-volume concentration in the $x-z$ plane along the center of the channel. A distribution of average particle sizes in the $x-z$ plane is similarly shown in Figure 13. These values are computed as $(\sum d_k)/N_{kmax}$, where d_k is a diameter of a particle occupying a cell k in the region, and N_{kmax} is the total number of cells occupied by particles in the region.

Vertical distributions of particle-volume concentrations of each size and average particle sizes are shown in Figure 14. These figures depicted vertical bed structures of antidune beds at $x = 7$ m where large particles formed clusters on the bed and at $x = 9$ m where they did not. Figures 11, 13, and 14 show that particle-volume concentrations were nearly 0.8 in the lower part of the bed. At the crown of antidunes ($x = 7$ m), particle-volume concentrations gradually decreased from about 0.15 m to the vertical upward direction. Porosities of the bed surface were considerably large there. In contrast,

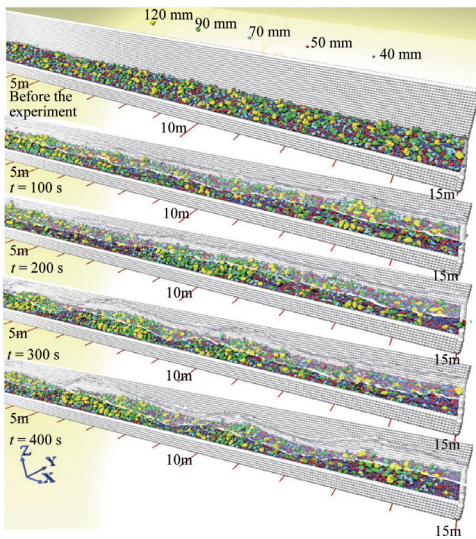


Figure 5. Temporal and spatial variations of bed surfaces.

Table 2. Temporal variations of hydrodynamic conditions.

Time	Depth (m)			Average velocity (m/s)			Fr		
	Minimum	Average	Maximum	Minimum	Average	Maximum	Minimum	Average	Maximum
$t = 100$ s	0.208	0.236	0.259	1.93	2.12	2.41	1.22	1.40	1.69
$t = 200$ s	0.219	0.258	0.307	1.63	1.95	2.29	0.94	1.24	1.56
$t = 300$ s	0.212	0.258	0.370	1.35	1.97	2.36	0.71	1.26	1.64
$t = 400$ s	0.200	0.268	0.414	1.21	1.93	2.50	0.60	1.22	1.78

particle-volume concentrations sharply decreased from about 0.1 m to the vertical upward direction at the trough of antidunes ($x = 9$ m). Porosities of the bed surface are relatively small. Therefore, particle-volume concentrations of troughs at antidunes were high where few large particles located on the bed surface.

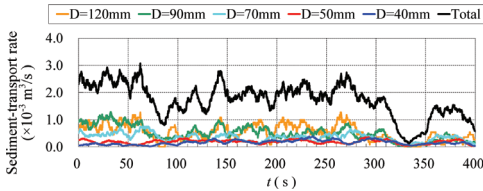


Figure 6. Temporal variations of sediment-transport rates.

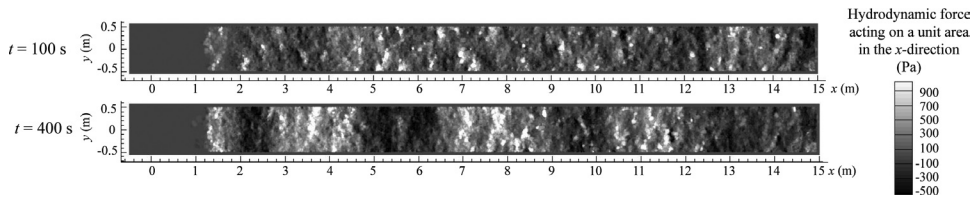


Figure 7. Hydrodynamic forces acting on a unit area in the x - y plane.

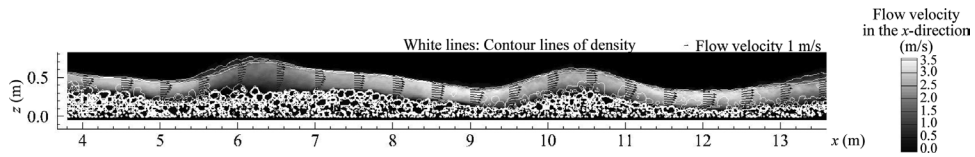


Figure 8. Flow in the center of the channel (Values are averaged in $t = 390$ s \sim $t = 400$ s).

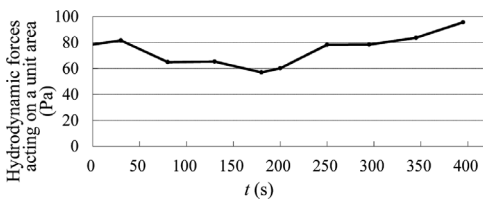


Figure 9. Temporal variations of averaged hydrodynamic forces acting on particles in a unit area.

5 EFFECT OF CONTACT FORCES ON PARTICLE MOTIONS AND BED STRUCTURES

5.1 Effect of contact forces on vertical structures of beds

We understood that the bed came to be stable through particle sorting on the bed surface caused by collisions among particles in different sizes. Figure 15 shows relationships between particle contact forces in the x -direction and the z -direction, which clarifies directions of contact forces in collisions. Particle-collision velocities which were larger than 0.1 m/s were used as sampling data of the figure. If these criteria of samples were the momentum, particle-velocity criteria of the smallest particles were 27 times larger than the largest particles, because the mass of the smallest particles was $1/27$

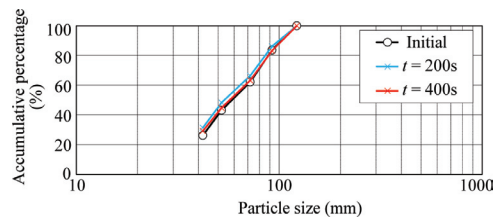


Figure 10. Temporal variations of the particle size distribution on the bed surface.

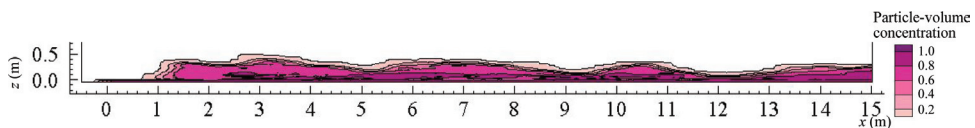


Figure 11. Distribution of particle-volume concentrations in the center of the channel at $t = 400$ s.

times ($0.04^3/0.12^3$) as much as that of the largest particles. However, small particles would not move so fast (Fukuda et al. 2013). Therefore, we selected a particle velocity as the criteria of samples to investigate contact forces among particles in motions.

Contact forces were nondimensionalized by submerged weights of particles. Contact forces in the z -direction of larger particles were great compared to those in the x -direction. The reasons are explained as follows: Small particles in a cloud of moving particles drop into gaps among particles easily. In contrast, large particles do not into gaps because of being supported by surrounding particles. Therefore, the larger particles were, the greater vertical components of contact forces were. There are differences between action directions of contact forces of particles in different sizes, and larger particles can move in upper levels of the bed surface. This is the mechanism of particle sorting on the movable bed.

Effects of particle-volume concentrations on particle motions were investigated. Relationships between particle-volume concentrations and ratios of velocities before collisions to after collisions (v_2/v_1) are shown in Figure 16 where v_1 and v_2 are velocities in the x -direction before and after collisions, respectively. The ratios (v_2/v_1) decreased with the increase in particle-volume concentrations.

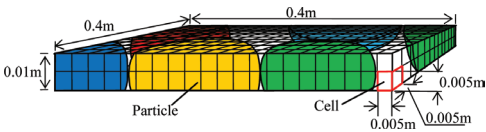


Figure 12. Region for measurement of particle-volume concentration and average particle size.

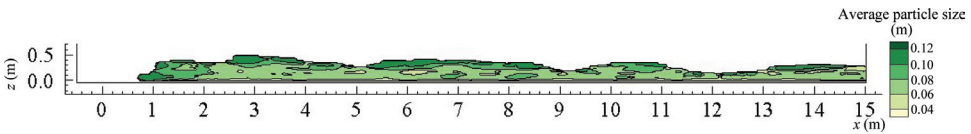


Figure 13. Distribution of average particle size in the center of the channel at $t = 400$ s.

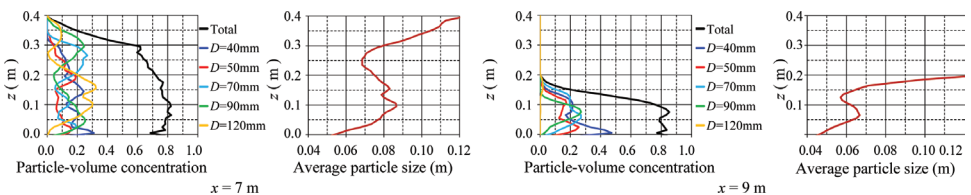


Figure 14. Vertical distributions of particle-volume concentrations of each size and average particle size.

This means that particles velocities decreased by particle collisions.

Relationships between stabilization of the bed and particle sorting on the bed surface are considered. We found that large particles moving on the bed surface received contact forces in the upward direction more easily than small particles in collisions and moved upper positions on the bed surface. Large particles moving in the upper position of the bed surface are not so many, and particle-volume concentrations are relatively small. Protruding large particles are easy to be transported by flows and to stop by collisions with stationary large particles on the bed surface. Then, larger particles form clusters and increase particles volume concentrations at the bed. In this manner, all particles on the bed surface come to be in relatively high volume concentrations and to resist against particle collisions and hydrodynamic forces. This mechanism leads to stable bed structures in gravel-bed rivers.

5.2 Contact forces at the time of incipient and settling motions

The x -direction particle velocities, contact forces, and hydrodynamic forces nondimensionalized by submerged weight of particles at the time of incipient and settling motions are shown in Figure 17. There are positive and negative contact forces. Positive and negative contact forces are forces which particles receive in collision with upstream particles and receive from downstream particles supporting them, respectively. On positive contact forces, small particles received larger contact forces than hydrodynamic forces and large particles did larger hydrodynamic forces than contact forces. The difference is explained as follows: Particle-volume concentrations were large in the lower part of the

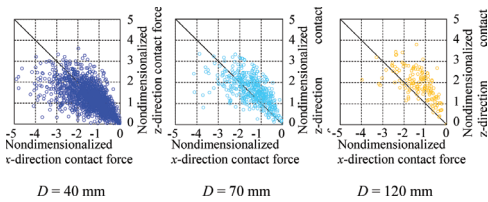


Figure 15. Directions of contact forces acting on particles in motion.

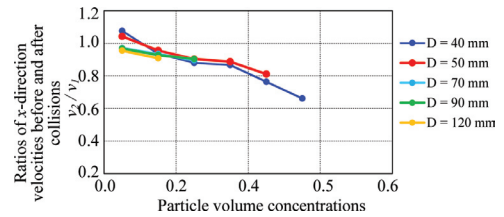


Figure 16. Relationships between particle-volume concentrations and ratios of particle velocities before collisions to after collisions.

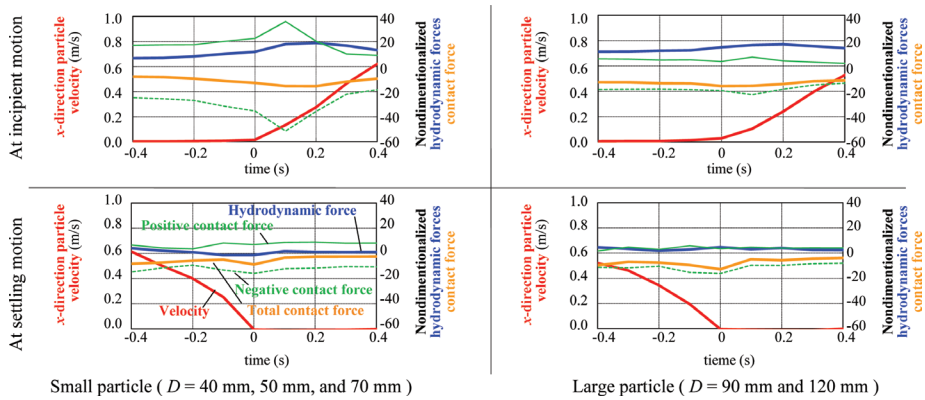


Figure 17. Time variations of particle velocities, hydrodynamic forces and contact forces at incipient and settling motions.

bed surface where many small particles rested in being sandwiched by other particles. Small particles received larger positive contact forces compared to large particles at the time of incipient motions. This is because small particles often collide with moving large particles. Thus, contact forces from relatively large particles are essential for incipient motions of small particles. In contrast, large particles rarely received contact forces from larger particles. Large particles started to move by receiving larger hydrodynamic forces than contact forces.

Hydrodynamic forces acting on large particles and small particles were considerably small at the time of settling compared to that at incipient motion because flows decelerated on upstream slopes of antidunes and a large number of particles settled there. These results show that proper estimations of momentum exchanges and collisions among particles in different sizes are required for predictions of sediment transport in gravel-bed rivers.

6 CONCLUSIONS

Numerical movable-bed experiments were conducted by using numerical movable-bed channel

with particles in different sizes and shapes. The following main conclusions were obtained.

1. Effects of hydrodynamic forces and contact forces of particle in different sizes were clarified by focusing on particle motions and vertical structures of movable-beds.
2. Contact forces in collisions make large particles move vertical upward compared to small particles and large particles move over small particles because small particles drop into gaps among particles.
3. Particle collisions bring a great impact on incipient motions of particles. Ratios of contact forces to hydrodynamic forces at incipient motions of small particle are higher than those of large particles.
4. Large particles moving in upper positions of the bed surface are not so many and particle-volume concentrations are relatively small. Protruding large particles are easy to be transported by flows and to stop by collisions with stationary large particles on the bed surface.
5. Mechanisms of sorting and stabilization of the bed surface were clarified on the basis of motions of particles in different sizes.

REFERENCES

- Cundall, P.A. & Strack, O.D.L. 1979. A discrete numerical model for granular assemblies. *Geotechnique* 29 (1): 47–65.
- Fukuoka, S. & Abe, T. 2007. Mechanism of low water channel formation and the role of grain-size distribution in gravel-bed rivers, *10th International Symposium on River Sedimentation, Moscow, Russia*.
- Fukuda, T. Fukuoka, S. & Uchida, T. 2012. Three-dimensional numerical modeling for the motion of stones with different sizes and shapes in streams. *10th International Conference on Hydroscience & Engineering, Orlando, USA*.
- Fukuda, T. Fukuoka, S. & Uchida, T. 2013. Three-dimensional motions in numerical movable bed channel with particles of various shapes and sizes. *12th International Symposium on River Sedimentation, Kyoto, Japan*.
- Harada, E. Gotoh, H. & Tsuruta, N. 2013. Distribution of shear stress in oscillatory sheet-flow layer by LES. *Journal of JSCE, B2 (Costal Engineering)* 69(2): I_556-I_560. in Japanese.
- Hendrick, R.R. Ely, L.L. & Papanicolaou, A.N. 2010. The role of hydrologic processes and geomorphology on the morphology and evolution of sediment clusters in gravel-bed rivers. *Geomorphology* 114: 483–496.
- Matsushima, T. Katagiri, J. Uesugi, K. Tsuchiyama, A. & Nakano, T. 2009. 3D shape characterization and image-based DEM simulation of the lunar soil simulant FJS-1. *J. Aerospace Engineering* 22(1): 15–23.
- Millane, R.P. Weir, M.I. & Smart, G.M. 2006. Automated analysis of imbrication and flow direction in alluvial sediments using laser-scan data. *Journal of Sedimentary Research* 76: 1049–1055.
- Osada, K. & Fukuoka, S. 2010. Analysis of two-dimensional riverbed variation in channels with stony beds. *11th International Symposium on River Sedimentation Stellenbosch South Africa*.
- Truong, H. Nguyen, A. Sugimoto, H. & Wells, J. 2007. Fictitious-domain simulations of bedload transport; free-surface flow in a rotating tumbler. *Annual Journal of Hydraulic Engineering, JSCE* 51: 157–162.
- Tsuji, Y. Tanaka, T. & Ishida, T. 1992. Lagrangian numerical simulation of plug flow of cohesionless particles in a horizontal pipe. *Powder Technology* 71; 239–250.
- Ushijima, S., Fukutani, A. & Makino, O. 2008. Prediction method for movements with collisions of arbitrary-shaped objects in 3D free-surface flows. *JSCE Journal B* 64(2): 128–138. in Japanese.